

above examine relatively simple binary systems, where only a single type of DNA sticky end duplex is created. However, because of the polyvalent nature of the DNA-NPs and the base sequence programmability of DNA, one is not necessarily restricted to a single type of favorable particle interaction in a given lattice. By cofunctionalizing a nanoparticle with different linkers that contain different base sequences, multiple sequence-specific DNA duplex interactions are possible (Fig. 4A). This is an inherent distinction and potential advantage of using a sequence-programmable linker such as DNA, as opposed to entropy- or charge-dominated assembly processes.

This rule was tested by cofunctionalizing a nanoparticle with two different linkers: one that bore a self-complementary sticky end, and one that bore a sticky end sequence complementary to the sticky ends of a second particle. In this system, the cofunctionalized particle (blue particle, Fig. 4A) exhibited an attractive force with respect to all particles encountered in the system, whereas the second particle (red particle, Fig. 4A) was only attracted to the first particle type. When the hydrodynamic radius size ratio of the two NPs was ~0.3 to 0.4, the sticky ends were presented at the correct distances from the particle surface to form a NaCl lattice (Fig. 4B); that is, the self-complementary and non-self-complementary linkers were both at a position to form duplexes in this crystallographic arrangement. Furthermore, when the inorganic core sizes were the same on both DNA-NPs, the particles formed a simple cubic lattice, as defined by the positions of the inorganic cores (Fig. 4C). Although NaCl and simple cubic structures are presented as the first examples of this multivalent strategy, one can envision even more sophisticated and complex systems (such as lattices with three or more nanoparticle components) using multiple DNA-programmed NP interactions.

We have presented a set of basic design rules for synthesizing a diverse array of nanoparticle superlattices using DNA as a synthetically programmable linker. These rules provide access to an easily tailorable, multifaceted design space in which one can independently dictate the crystallographic symmetry, lattice parameters, and particle sizes within a lattice. This in turn enables the synthesis of many different nanoparticle superlattices that cannot be achieved through other methodologies. Indeed, superlattices that do not follow the well-known hard-sphere packing parameter rules defined by Schiffrin and co-workers (6) and Murray and co-workers (8, 24) can easily be assembled as thermodynamically stable structures over a range of nanoparticle sizes and lattice parameters. The understanding gained from the use of these rules will both inform and enable future assembly efforts, allowing for the construction of new crystallographic arrangements that have emergent properties for use in the fields of plasmonics (14, 25, 26), photonics (27), catalysis (28, 29), and potentially many others.

References and Notes

1. L. Pauling, *The Nature of the Chemical Bond* (Cornell Univ. Press, Ithaca, NY, ed. 3, 1960).
2. C. A. Mirkin, R. L. Letsinger, R. C. Mucic, J. J. Storhoff, *Nature* **382**, 607 (1996).
3. S.-J. Park, A. A. Lazarides, J. J. Storhoff, L. Pesce, C. A. Mirkin, *J. Phys. Chem. B* **108**, 12375 (2004).
4. S. Y. Park *et al.*, *Nature* **451**, 553 (2008).
5. D. Nykypanchuk, M. M. Maye, D. van der Lelie, O. Gang, *Nature* **451**, 549 (2008).
6. C. J. Kiely, J. Fink, M. Brust, D. Bethell, D. J. Schiffrin, *Nature* **396**, 444 (1998).
7. A. M. Kalsin *et al.*, *Science* **312**, 420 (2006); 10.1126/science.1125124.
8. E. V. Shevchenko, D. V. Talapin, N. A. Kotov, S. O'Brien, C. B. Murray, *Nature* **439**, 55 (2006).
9. S. Srivastava *et al.*, *Science* **327**, 1355 (2010); 10.1126/science.1177218.
10. S. Wong, V. Kitaev, G. A. Ozin, *J. Am. Chem. Soc.* **125**, 15589 (2003).
11. Y. Zhao *et al.*, *Nat. Mater.* **8**, 979 (2009).
12. C.-L. Chen, N. L. Rosi, *Angew. Chem. Int. Ed.* **49**, 1924 (2010).
13. Z. Nie, A. Petukhova, E. Kumacheva, *Nat. Nanotechnol.* **5**, 15 (2010).
14. M. R. Jones, K. D. Osberg, R. J. Macfarlane, M. R. Langille, C. A. Mirkin, *Chem. Rev.* **111**, 3736 (2011).
15. R. J. Macfarlane *et al.*, *Proc. Natl. Acad. Sci. U.S.A.* **106**, 10493 (2009).
16. R. J. Macfarlane *et al.*, *Angew. Chem. Int. Ed.* **49**, 4589 (2010).
17. M. R. Jones *et al.*, *Nat. Mat.* **9**, 913 (2010).
18. H. Xiong, D. van der Lelie, O. Gang, *Phys. Rev. Lett.* **102**, 015504 (2009).
19. See supporting material on Science online.
20. L. V. Woodcock *et al.*, *Nature* **385**, 141 (1997).
21. O. Zhou *et al.*, *Nature* **351**, 462 (1991).
22. V. A. Bloomfield, D. M. Crothers, I. Tinoco, *Nucleic Acids: Structures, Properties, and Functions* (University Science Books, Sausalito, CA, 2000).
23. A. V. Tkachenko, *Phys. Rev. Lett.* **89**, 148303 (2002).
24. M. I. Bodnarchuk, M. V. Kovalenko, W. Heiss, D. V. Talapin, *J. Am. Chem. Soc.* **132**, 11967 (2011).
25. K. L. Kelly, E. Coronado, L. L. Zhao, G. C. Schatz, *J. Phys. Chem. B* **107**, 668 (2002).
26. J. A. Fan *et al.*, *Science* **328**, 1135 (2010).
27. K. J. Stebe, E. Lewandowski, M. Ghosh, *Science* **325**, 159 (2009).
28. A. T. Bell, *Science* **299**, 1688 (2003).
29. J. Grunes, J. Zhu, E. A. Anderson, G. A. Somorjai, *J. Phys. Chem. B* **106**, 11463 (2002).

Acknowledgments: Supported by the Defense Research & Engineering Multidisciplinary University Research Initiative of the Air Force Office of Scientific Research and by the U.S. Department of Energy Office of Basic Energy Sciences [award DE-SC0000989; Northwestern University (NU) Non-equilibrium Energy Research Center] (C.A.M. and G.C.S.); a National Security Science and Engineering Faculty Fellowship from the U.S. Department of Defense (C.A.M.); a NU Ryan Fellowship (R.J.M.); and a NU Ryan Fellowship and a NSF Graduate Research Fellowship (M.R.J.). Portions of this work were carried out at the DuPont-Northwestern-Dow Collaborative Access Team (DND-CAT) beamline located at Sector 5 of the Advanced Photon Source (APS). DND-CAT is supported by E. I. DuPont de Nemours & Co., Dow Chemical Company, and the state of Illinois. Use of the APS was supported by the U.S. Department of Energy, Office of Science, Office of Basic Energy Sciences, under contract DE-AC02-06CH11357. The transmission electron microscope work was carried out in the EPIC facility of the NU Atomic and Nanoscale Characterization Experimental Center, which is supported by NSF-NSEC, NSF-MRSEC, Keck Foundation, the state of Illinois, and NU. Ultrathin sectioning was carried out at the NU Biological Imaging Facility, supported by the NU Office for Research.

Supporting Online Material

www.sciencemag.org/cgi/content/full/334/6053/204/DC1
Materials and Methods
SOM Text
Figs. S1 to S31
Tables S1 and S2
References (30–44)

29 June 2011; accepted 25 August 2011
10.1126/science.1210493

Conical Intersection Dynamics in NO₂ Probed by Homodyne High-Harmonic Spectroscopy

H. J. Wörner,^{1,2*} J. B. Bertrand,¹ B. Fabre,³ J. Higuier,³ H. Ruf,³ A. Dubrouil,³ S. Patchkovskii,¹ M. Spanner,¹ Y. Mairesse,³ V. Blanchet,⁴ E. Mével,³ E. Constant,³ P. B. Corkum,¹ D. M. Villeneuve¹

Conical intersections play a crucial role in the chemistry of most polyatomic molecules, ranging from the simplest bimolecular reactions to the photostability of DNA. The real-time study of the associated electronic dynamics poses a major challenge to the latest techniques of ultrafast measurement. We show that high-harmonic spectroscopy reveals oscillations in the electronic character that occur in nitrogen dioxide when a photoexcited wave packet crosses a conical intersection. At longer delays, we observe the onset of statistical dissociation dynamics. The present results demonstrate that high-harmonic spectroscopy could become a powerful tool to highlight electronic dynamics occurring along nonadiabatic chemical reaction pathways.

The outcome of chemical reactions is determined by the valence electronic structure of molecules. Therefore, the elucidation of elementary reaction mechanisms requires an understanding of the valence electron dynamics. Recently developed techniques that are efficient

in probing valence electron dynamics include attosecond transient absorption (1), extreme ultraviolet photoelectron spectroscopy (XUV-PES) (2), high-order harmonic spectroscopy (HHS) (3–5) and strong-field ionization (6). Both time-resolved PES (7) and time-resolved HHS are

sensitive to valence electron dynamics through the molecular photoionization matrix elements.

Electronic dynamics in molecules are particularly challenging to observe when they are strongly coupled to nuclear dynamics. Such situations often arise in polyatomic molecules where conical intersections induce very rapid radiationless transitions at particular nuclear configurations (see inset of Fig. 1) (8, 9). These features channel electronic excitation into atomic motion in such diverse contexts as the primary steps of vision (10) and the dynamics underlying electron transfer and the photostability of DNA bases (11).

Here, we show that high-harmonic spectroscopy reveals the variations in electronic character during the conical intersection dynamics and the subsequent dissociation of nitrogen dioxide (NO_2). We chose NO_2 , a radical, because of its model status for theories of unimolecular dissociation (12–14) and conical intersection dynamics (15–19). Our results translate the previously recognized sensitivity of HHS to electronic structure into a tool for elucidating chemical reaction dynamics.

High-harmonic spectroscopy can be factored into three steps: removal of an electron by an intense femtosecond laser field, acceleration of the electron in the laser field, and photorecombination (20, 21). Each step contributes an amplitude and a phase to the emitted XUV radiation (22–24, 20, 25). The measurement relies on a coherent detection scheme in a transient grating geometry, using unexcited molecules as a local oscillator (4, 5). It is thus sensitive to both amplitude and phase of the photorecombination matrix elements, a quantity that has recently attracted a lot of interest (26, 27). Time-resolved HHS is thus related to time-resolved PES but differs in its sensitivity to the continua associated with different ionic states. PES projects the molecular wave packet onto a set of ionic states, influenced by resonances, Franck-Condon factors, and dissociative ionization. HHS involves recombination from an energetic continuum electron with one or a few of the lowest ionic states that were selected by tunneling ionization.

A schematic representation of the potential energy surfaces of NO_2 is shown in Fig. 1. In the \tilde{X}^2A_1 electronic ground state, NO_2 possesses a bent equilibrium geometry and the dominant electronic configuration in the two highest occupied orbitals is $(b_2)^2(a_1)^1$. Single-photon absorption at 400 nm excites the molecule to the \tilde{A}^2B_2

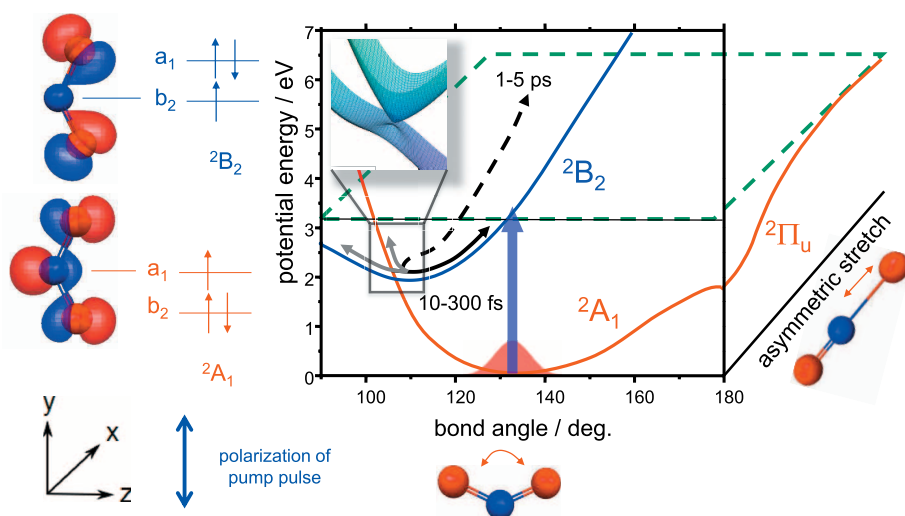


Fig. 1. Schematic representation of the potential energy surfaces of the ground \tilde{X}^2A_1 and excited \tilde{A}^2B_2 electronic states of NO_2 . The dominant electronic configuration in the two highest-lying molecular orbitals is shown for each state on the left. The orbitals are represented by isoamplitude surfaces of the wave function with color-coding of the sign. After excitation by a 400-nm pump pulse (blue arrow), the wave packet initially moves along the bending coordinate, crosses the conical intersection (shown in the top left inset) several times during the first 100 fs, and spreads along the asymmetric-stretch coordinate. Wave-packet population that has returned to the ground electronic state and possesses an energy above 3.1155 eV (green dashed line) dissociates on the picosecond time scale (dashed arrow).

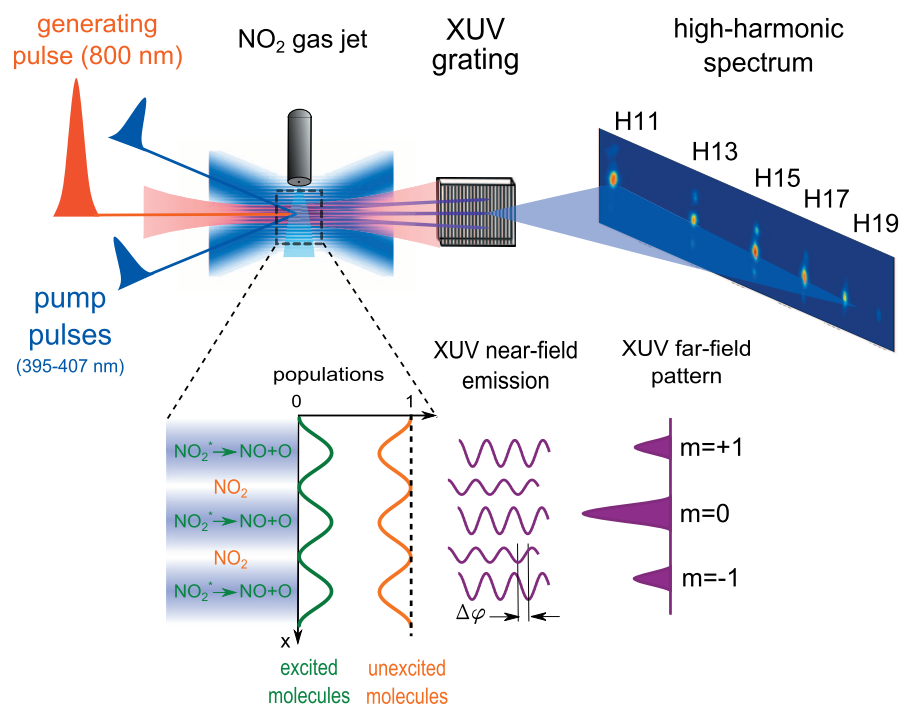


Fig. 2. Experimental setup for high-harmonic transient grating spectroscopy as first described in (4). The transient grating creates a spatially modulated population of excited molecules accompanied by a depletion of the unexcited molecules. The periodic structure results in a modulation of amplitude and phase of the XUV emission in the near field that leads to first-order diffraction in the far field. An XUV grating disperses the radiation in one dimension while the beam freely diverges in the other dimension. With $r(\cos(kx) + 1)$ being the spatially modulated excitation fraction, the signal in $m = 0$ is given by $I_{m=0} = |(1 - r)d_g e^{i\phi_g} + r d_e e^{i\phi_e}|^2$ and that in $m = \pm 1$ by $I_{m=\pm 1} = \frac{r^2}{4} |d_e e^{i\phi_e} - d_g e^{i\phi_g}|^2$, where the symbols are defined in the text relating to Eq. 1.

¹Joint Laboratory for Attosecond Science, National Research Council of Canada and University of Ottawa, 100 Sussex Drive, Ottawa, Ontario, Canada K1A 0R6. ²Laboratorium für Physikalische Chemie, Eidgenössische Technische Hochschule Zürich, Wolfgang-Pauli-Strasse 10, 8093 Zürich, Switzerland. ³Centre Lasers Intenses et Applications, Université de Bordeaux, CEA, CNRS, UMR5107, 351 Cours de la Libération, 33405 Talence, France. ⁴Laboratoire Collisions Agrégats Réactivité (IRSAMC), UPS, Université de Toulouse, F-31062 Toulouse, France and CNRS, UMR 5589, F-31062 Toulouse, France

*To whom correspondence should be addressed. E-mail: woerner@phys.chem.ethz.ch

state of dominant configuration $(b_2)^1(a_1)^2$. The \tilde{A}^2B_2 excited state forms a conical intersection with the ground state (see inset of Fig. 1). Wave-packet calculations have shown that within the first femtoseconds after excitation, the nuclear wave packet moves along the bending coordinate toward the conical intersection, where it can either cross the intersection and remain on the same diabatic surface or else stay in the upper cone of the intersection and thus change the diabatic surface (gray arrows in Fig. 1) (15–18). After a few hundred femtoseconds, the nuclear wave packet returns to the electronic ground state through internal conversion. If the energy of the absorbed photon lies above the first dissociation limit at 3.1155 eV (397.95 nm) (all quoted wavelengths are vacuum values), the molecule dissociates into NO ($X^2\Pi_Q$) and O (3P_J) on the picosecond time scale (dotted arrow in Fig. 1). Previous studies using laser-induced fluorescence have characterized the picosecond dissociation in detail (14, 28). However, the femtosecond conical intersection dynamics has been largely obscured by competing multiphoton processes (19), requiring elaborate coincidence detection methods (29).

The experimental setup is illustrated in Fig. 2. We excite NO₂ in a transient grating formed from two synchronized 400-nm laser pulses and probe its dynamics by high-harmonic generation from an 800-nm, 32-fs laser pulse (4, 30). The excitation pulses are generated either in a 2-mm-thick β -barium borate (BBO) crystal, providing 160-fs pulses of 1-nm spectral width tunable from 395 to 407 nm or in a 100- μ m-thick BBO crystal, giving 40-fs pulses of 5-nm spectral width. The combination of the transient grating with an XUV monochromator allows us to spectrally resolve the high harmonics (H11 to H21 in this experiment) and to measure both the undiffracted ($m = 0$) and diffracted ($m = \pm 1$) components of each harmonic order. The signal observed in $m = 0$ is equivalent to a measurement done in a collinear pump-probe geometry, whereas the diffracted signal results from an interference between equal populations of excited and unexcited molecules (4).

We first discuss the picosecond photodissociation dynamics, which show that our measurement is dominated by single-photon absorption. The measurements were done with the 160-fs pulses, but we have obtained fully consistent results with the 40-fs pulses. The dynamics observed after excitation by pump pulses centered at 407 or 397.2 nm are shown in Fig. 3, A and C, respectively. Figure 3A shows a step-like decrease of the undiffracted XUV radiation and a corresponding increase of the diffracted intensity. The total ion yield, measured simultaneously and shown in Fig. 3B, increases, whereas the high-order harmonic signal decreases; this indicates a destructive interference between harmonics emitted by the ground state and those emitted by the excited state (4, 5). In this scan, performed with a 200-fs delay step, there is no

signature of any regular dynamics. Figure 3, C and D, however, show exponential growth or decay on the picosecond time scale, following the step-like variations.

The combined information from Fig. 3 shows that the step-like response to excitation below threshold characterizes electronic excitation without dissociation (Fig. 3, A and B), whereas the exponential variation of the signal in Fig. 3, C and D shows the unimolecular decomposition of NO₂. To quantify these observations, we introduce a simple model. When excitation takes

place below threshold, the radiated XUV field can be described as in Eq. 1

$$E_{\text{XUV}}(\Omega) = (1 - r)d_g e^{i\phi_g} + r d_e e^{i\phi_e} \tag{1}$$

where r is the spatially modulated fraction of excited molecules, and d_g , d_e and ϕ_g , ϕ_e are the high-harmonic amplitudes and phases of the ground or excited molecular states, respectively. When the excitation frequency exceeds threshold, the excited molecules can undergo dissociation into NO(²Π)+O(³P) that, together, emit harmonics

Table 1. Molecular parameters for strong-field ionization and high-harmonic generation, determined by fitting Eqs. 1 and 2 to the experimental data shown in Fig. 3, A to D. The excitation fraction r has been determined from the experimental parameters as described in the text.

Species	r	iI/I_g	H13		H15		H17	
			d/d_g	$ \phi - \phi_g (\text{rad})$	d/d_g	$ \phi - \phi_g (\text{rad})$	d/d_g	$ \phi - \phi_g (\text{rad})$
NO ₂ ⁺ (407 nm)	0.15	4.5	3.0	2.03	2.3	2.02	1.2	2.24
NO ₂ ⁺ (397 nm)	0.15	4.5	3.2	1.94	2.1	1.92	1.1	4.22
NO + O (397 nm)	0.15	2.3	6.1	2.09	4.1	2.00	1.4	1.87

$\tau = 2.71 \pm 0.15$ ps

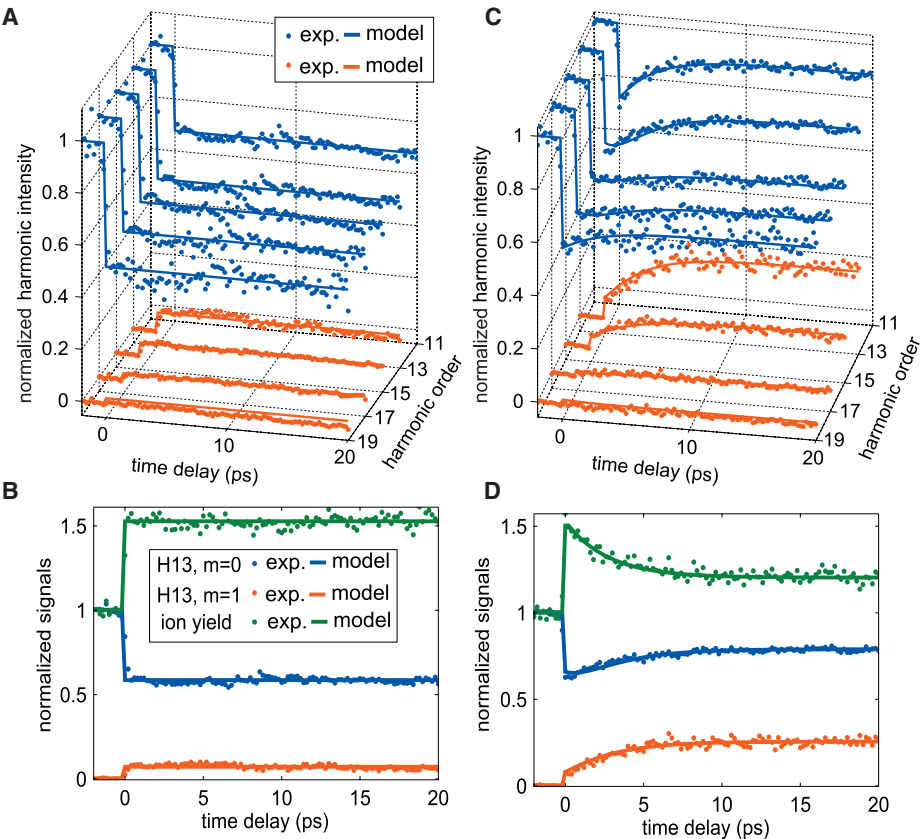


Fig. 3. High-harmonic and ion yields as a function of delay between two synchronized near-UV pump pulses setting up a transient grating and an 800-nm probe pulse generating high harmonics in the excited sample. (A) The yield of diffracted (red dots) and undiffracted (blue dots) high-harmonic signals, normalized to the undiffracted signal at negative pump-probe delays, for excitation by 407-nm pump pulses. The full lines represent the results of the theoretical model described in the text. (B) H13, $m = 0$, and $m = 1$ from (A) together with the total ion yield measured in parallel to the experiment (green dots) and the theoretical model (green line). (C and D) The same observables as (A and B), but for a pump pulse centered at 397.2 nm. Polarization of pump and probe are parallel. The typical pump energy is 10 μ J to minimize multiphoton processes.

with a resultant amplitude d_t and phase ϕ_t . The radiated XUV field is then given by Eq. 2

$$E_{\text{XUV}}(\Omega, t) = (1 - r)d_g e^{i\phi_g} + r e^{-t/\tau} d_e e^{i\phi_e} + r(1 - e^{-t/\tau}) d_t e^{i\phi_t} \quad (2)$$

where t is the time elapsed since excitation and τ is the time constant of the unimolecular dissociation.

To extract the relevant parameters from the measurement, both the diffracted and undiffracted high-harmonic signals are normalized by the signal measured in the absence of excitation (namely, $|d_g|^2$). We calculate the excited state fraction from the measured pulse energy, focal spot size, and the known absorption cross section of NO_2 and determine the unknown parameters in a global nonlinear least-squares fit. The determined parameters are given in Table 1, and the corresponding fit is shown as full lines in Fig. 3, A to D. The total ion yield is represented by equations similar to Eqs. 1 and 2 but with phases set to zero.

The global fit to all high-harmonic orders and ion signals in Fig. 3, B and D, provides a

time constant $\tau = 2.71 \pm 0.15$ ps, in agreement with the 2.78 ps measured previously at room temperature (14). The deep modulation of the signals demonstrates that the probed dynamics are dominated by one-photon absorption, which is in general difficult to achieve in femtosecond time-resolved measurements on molecules because of multiphoton processes (19). The strong-field ionization probability of vibrationally excited NO_2 molecules in the electronic ground state is larger than that of unexcited molecules [vertical ionization potential (I_p) =

11.2 eV] by a factor of $\left(\frac{I}{I_g}\right) \approx 4.5$. The ionization

rate of $\text{NO} + \text{O}$ (dominated by NO because the vertical I_p values are 9.2 and 13.8 eV, respectively) exceeds that of the unexcited molecules by a factor of ≈ 2.3 . The relative high-harmonic amplitudes are larger for the excited molecules, especially for low harmonic orders, and the phase shift is substantial, as expected from the observed destructive interference. The relative amplitudes for the $\text{NO} + \text{O}$ pair decrease particularly fast

with increasing harmonic order, as expected from the lower cutoff of the harmonic emission from NO . We thus conclude that the observed high-harmonic signal is dominated by single-photon excitation, in contrast to previous femtosecond time-resolved measurements that reported oscillatory components of periods in the range of 500 to 850 fs (31–33). The latter were indeed attributed to multiphoton excitations to higher-lying electronic states that would not emit high harmonics owing to their low binding energies.

In the following, we exploit this property to investigate the hitherto unobserved femtosecond dynamics of NO_2 in the \tilde{A}^2B_2 state. These measurements were done with 40-fs excitation pulses centered at 401 nm. The experimental results measured with cross-polarized laser pulses are shown in Fig. 4, A and B. Fig. 4A shows the undiffracted and diffracted signals measured in harmonics 11 through 17 (blue and red dots, respectively), and Fig. 4B shows the same quantities for H15 and H16 (green line). The latter allows an accurate determination of the zero time delay and the cross-correlation function (34). Whereas the $m = 0$ order decreases smoothly over the duration of the cross correlation, the diffracted order ($m = 1$) increases and reaches a maximum at a pump-probe delay of 35 fs. The diffracted signal subsequently decreases and reaches a minimum around 70 fs, followed by another maximum at 130 fs. Further modulations with decreasing contrast are observed at longer pump-probe delays. As we show and discuss in fig. S2 and the accompanying text, no modulations are observed in parallel polarization.

These oscillations, observed in the diffracted XUV radiation, are a fingerprint of the electronic dynamics of the molecule taking place around the conical intersection, as illustrated schematically in Fig. 4D. In the bright zones of the transient grating, the electronic character of the excited molecules oscillates between \tilde{X}^2A_1 and \tilde{A}^2B_2 . When the molecule is in the \tilde{X}^2A_1 state, the near-field variation of the high-harmonic emission is much smaller for most molecular geometries than when it is in the \tilde{A}^2B_2 state, which we detect as a variation of the intensity of diffracted radiation [see section VI of the supporting online material (SOM)].

To rationalize these observations, we introduce a simple model based on diabatic electronic states and coordinate-independent transition moments (more detailed calculations are given in the SOM). The total radiated XUV field is the coherent sum of contributions from the unexcited molecules (subscript g) and excited molecules in the two diabatic \tilde{A}^2B_2 and \tilde{X}^2A_1 states (Eq. 3)

$$E_{\text{XUV}}(\Omega, t) = [1 - r(t)]d_g e^{i\phi_g} + r_{\tilde{A}}(t)d_{\tilde{A}} e^{i\phi_{\tilde{A}}} + r_{\tilde{X}}(t)d_{\tilde{X}} e^{i\phi_{\tilde{X}}} \quad (3)$$

where $r(t) = r_{\tilde{A}}(t) + r_{\tilde{X}}(t)$ is the total fraction of excited molecules before dissociation takes

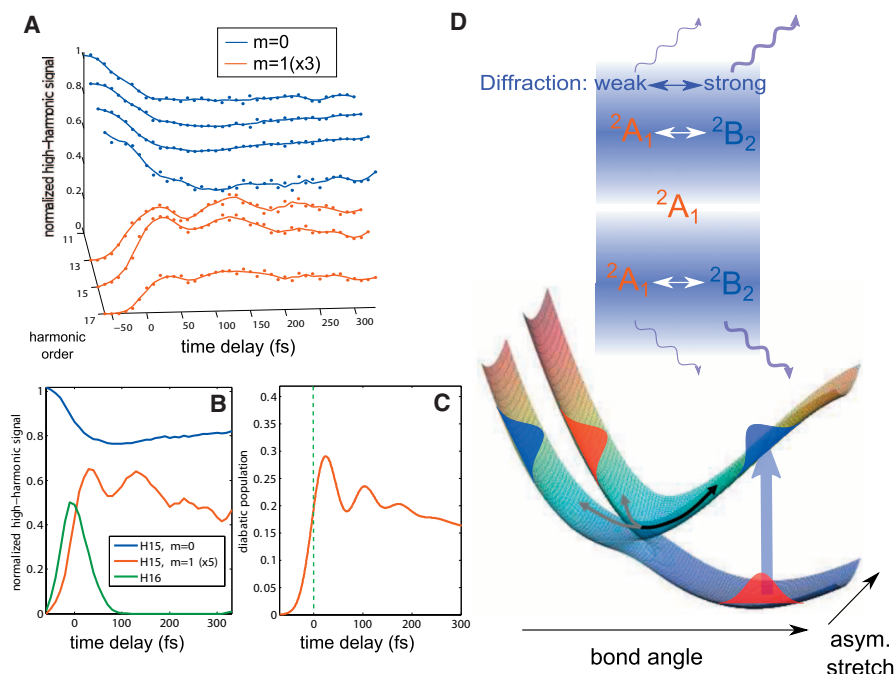


Fig. 4. (A) The high-harmonic yields after excitation by a pair of 10- μ J, 401-nm laser pulses in the undiffracted (blue) and diffracted orders (red) of the odd harmonics (H11 to H17). Experimental data points appear as dots and a three-point-smoothed version as lines. (B) The undiffracted (blue) and diffracted orders of H15 (red) and H16 (green line). (C) The diabatic excited state population from (17) convoluted with a 50-fs Gaussian cross-correlation function. (D) Illustration of how high-harmonic transient-grating spectroscopy probes the electronic character of the molecule during the conical intersection dynamics. The top illustrates the spatial intensity structure of the transient grating. The bottom shows schematically the lowest two potential energy surfaces of NO_2 . When the molecule is in the excited diabatic state (represented as a blue wave packet), the high-harmonic emission differs significantly from the unexcited (2A_1) molecules, leading to a large variation of high-harmonic amplitude and phase across the transient grating and thus to strong diffraction. When population is transferred into the ground diabatic state (red wave packet), the modulation depth of high-harmonic amplitude and phase across the transient grating, and therefore the diffracted intensity, decreases.

place. The intensity of the diffracted light is thus given by Eq. 4 (4)

$$I_{m=1}(\Omega, t) = \frac{1}{4} |r_{\tilde{A}}(t)(d_{\tilde{A}}e^{i\phi_{\tilde{A}}} - d_{\tilde{g}}e^{i\phi_{\tilde{g}}}) + r_{\tilde{X}}(t)(d_{\tilde{X}}e^{i\phi_{\tilde{X}}} - d_{\tilde{g}}e^{i\phi_{\tilde{g}}})|^2 \quad (4)$$

The high-harmonic amplitude is determined by the probabilities of ionization and recombination. The phase is determined by the phase accumulated by the bound state ($I_p \tau$), and the recombination phase (24), where τ stands for the transit time of the electron in the continuum (~1 to 1.7 fs). To the first order, ionization from either \tilde{A}^2B_2 or \tilde{X}^2A_1 involves the removal and recombination of an a_1 electron in the cross-polarized case (Fig. 1). The main difference is due to the $I_p \tau$ phase. The ground-state channel $^1A_1 \leftarrow ^2A_1$ has an I_p of 11.2 eV, whereas the main excited-state ionization channel $^3B_2 \leftarrow ^2B_2$ has an I_p that varies between 9.8 eV and 13.2 eV as a function of the bending coordinate. The relative phase difference $\Delta I_p \tau$ stays close to zero for the \tilde{X}^2A_1 state, whereas it is significantly larger (between 1 and 3 radians) for most geometries of the \tilde{A}^2B_2 state. Hence, in Eq. 4, $|d_{\tilde{A}}e^{i\phi_{\tilde{A}}} - d_{\tilde{g}}e^{i\phi_{\tilde{g}}}| \gg |d_{\tilde{X}}e^{i\phi_{\tilde{X}}} - d_{\tilde{g}}e^{i\phi_{\tilde{g}}}|$ and the time dependence of the diffracted signal will be dominated by HHG emission from the \tilde{A}^2B_2 state. It is thus sensitive to the temporal variation of the population in the \tilde{A}^2B_2 state, as illustrated in Fig. 4D. This conclusion is also supported by the detailed calculations described in the SOM.

The observed polarization dependence of the oscillations is a consequence of the electronic symmetries. Photoexcited molecules have their y axis (O-O axis) parallel to the polarization of the exciting field (Fig. 1). In the cross-polarized experiment, the emission from excited molecules is thus dominated by those probed along their z axis (C_2 axis). The same orientation also dominates the emission from the unexcited molecules, resulting in a sensitivity to the diabatic electronic state of the excited molecule (2B_2 versus 2A_1). In the case of parallel polarizations, the photoexcited molecules are being probed along their y axis, whereas the unexcited molecules are probed along their z axis. Therefore, the emission from excited molecules in both diabatic states differs significantly from that of the unexcited molecules, and the amount of diffracted light is sensitive only to the total population of excited molecules.

Because the electronic dynamics between \tilde{X}^2A_1 and \tilde{A}^2B_2 have not been observed experimentally before, we compare the measurements to recent quantum dynamical calculations on NO_2 (17, 18). These three-dimensional wave packet calculations have predicted characteristic oscillations in the diabatic populations over the first few hundred femtoseconds. The diabatic \tilde{A}^2B_2 population $r_{\tilde{A}}(t)$, convoluted with a 50-fs Gaussian cross-correlation function, is shown in Fig. 4C. Both the overall behavior and the distinct features observed in the diffracted high-harmonic signal are present in the calculated

diabatic state population. The first maximum occurs at a delay of 26 fs, the first minimum at 68 fs, and the second maximum at 106 fs. The modulations in the diffracted signal thus reflect the diabatic state population dynamics. Considering the complexity of the problem and the simplicity of our model, the agreement is remarkable. To exclude the possibility that the observed modulations result from a change of the strong-field-ionization rate of the molecule as a function of the nuclear coordinates, we have also measured the total ion yield in parallel to the high-harmonic yield and have not observed any modulation on top of the smooth increase (see fig. S3 and accompanying text).

Comparing the experimental and theoretical results, we can draw a qualitative picture of the evolution of the electronic structure of the molecule as it crosses the conical intersection. Photoexcitation prepares the wave packet on the upper diabatic state as shown in Fig. 4D. When it first approaches the conical intersection, it has little expansion along the asymmetric stretch coordinate (the b_2 mode responsible for vibronic coupling), and thus most of the amplitude traverses the intersection and remains on the same diabatic state [80% according to the wave packet calculation (17)]. This fraction, the diabatic wave packet, returns to the conical intersection with a significant spread along the bond-stretching coordinate, resulting in a strong transfer to the ground diabatic state. This leads to the first minimum in the diabatic state population around 60 fs. After two or three periods of motion along the bending coordinate, wave packet components from diabatic and adiabatic traversals interfere with each other and extend so significantly along the symmetric and asymmetric stretch coordinates that no appreciable motion of the wave packet average position can be defined for times longer than 200 fs (15, 17).

High-harmonic spectroscopy is a powerful probe of electronic dynamics in nonadiabatic processes. The homodyne interference of species in different electronic states has enabled us to distinguish multiple photochemical pathways—electronic excitation to bound states versus excitation followed by dissociation. The coherence of the high-harmonic emission also enabled us to extract amplitudes and phases of the various species occurring in the photochemical transformation and to learn how to interpret them. Temporal variations in the dominant electronic configuration of the photoexcited wave packet are manifested in a polarization dependence of the pump-probe signal, which is expected to be a powerful property in future studies of electronic dynamics.

We have thus demonstrated how to use high-harmonic spectroscopy to elucidate a complex photochemical process from the first femtoseconds that are governed by a conical intersection to the picosecond time scale where dissociation proceeds statistically. Our results on the femtosecond dynamics may be used in the future to check high-level quantum dynam-

ical calculations. We anticipate that this property will be of great value to femtochemistry and ultrafast imaging.

References and Notes

1. E. Goulielmakis *et al.*, *Nature* **466**, 739 (2010).
2. L. Nugent-Glandorf *et al.*, *Phys. Rev. Lett.* **87**, 193002 (2001).
3. W. Li *et al.*, *Science* **322**, 1207 (2008).
4. H. J. Wörner, J. B. Bertrand, D. V. Kartashov, P. B. Corkum, D. M. Villeneuve, *Nature* **466**, 604 (2010).
5. H. J. Wörner, J. B. Bertrand, P. B. Corkum, D. M. Villeneuve, *Phys. Rev. Lett.* **105**, 103002 (2010).
6. M. Meckel *et al.*, *Science* **320**, 1478 (2008).
7. C. Z. Bisgaard *et al.*, *Science* **323**, 1464 (2009).
8. W. Domcke, D. R. Yarkony, H. Köppel, Eds., *Conical Intersections: Electronic Structure, Dynamics and Spectroscopy*, vol. 15, *Advanced Series in Physical Chemistry* (World Scientific, Singapore, 2004).
9. P. H. Bucksbaum, *Science* **317**, 766 (2007).
10. D. Polli *et al.*, *Nature* **467**, 440 (2010).
11. T. Schultz *et al.*, *Science* **306**, 1765 (2004).
12. G. E. Busch, K. R. Wilson, *J. Chem. Phys.* **56**, 3626 (1972).
13. M. Quack, J. Troe, *Ber. Bunsenges. Phys. Chem.* **78**, 240 (1974).
14. S. I. Ionov, G. A. Brucker, C. Jaques, Y. Chen, C. Wittig, *J. Chem. Phys.* **99**, 3420 (1993).
15. F. Santoro, C. Petrongolo, *J. Chem. Phys.* **110**, 4419 (1999).
16. S. Mahapatra, H. Köppel, L. S. Cederbaum, P. Stampfl, W. Wenzel, *Chem. Phys.* **259**, 211 (2000).
17. Y. Arasaki, K. Takatsuka, *Chem. Phys.* **338**, 175 (2007).
18. Y. Arasaki, K. Takatsuka, K. Wang, V. McKoy, *J. Chem. Phys.* **132**, 124307 (2010).
19. I. Wilkinson, B. J. Whitaker, *Annu. Rep. Prog. Chem. Sect. C: Phys. Chem.* **106**, 274 (2010).
20. A.-T. Le, R. R. Lucchese, M. T. Lee, C. D. Lin, *Phys. Rev. Lett.* **102**, 203001 (2009).
21. M. V. Frolov *et al.*, *Phys. Rev. Lett.* **102**, 243901 (2009).
22. J. Itatani *et al.*, *Nature* **432**, 867 (2004).
23. T. Morishita, A.-T. Le, Z. Chen, C. D. Lin, *Phys. Rev. Lett.* **100**, 013903 (2008).
24. H. J. Wörner, H. Niikura, J. B. Bertrand, P. B. Corkum, D. M. Villeneuve, *Phys. Rev. Lett.* **102**, 103901 (2009).
25. H. J. Wörner, J. B. Bertrand, P. Hockett, P. B. Corkum, D. M. Villeneuve, *Phys. Rev. Lett.* **104**, 233904 (2010).
26. M. Swoboda *et al.*, *Phys. Rev. Lett.* **104**, 103003 (2010).
27. M. Schultze *et al.*, *Science* **328**, 1658 (2010).
28. B. Abel, B. Kirmse, J. Troe, D. Schwarzer, *J. Chem. Phys.* **115**, 6522 (2001).
29. A. Vredenburg, W. G. Roeterdink, M. H. M. Janssen, *J. Chem. Phys.* **128**, 204311 (2008).
30. Y. Mairesse *et al.*, *Phys. Rev. Lett.* **100**, 143903 (2008).
31. N. T. Form, B. J. Whitaker, L. Poisson, B. Soep, *Phys. Chem. Chem. Phys.* **8**, 2925 (2006).
32. D. Irimia, I. D. Petsalakis, G. Theodorakopoulos, M. H. M. Janssen, *J. Phys. Chem. A* **114**, 3157 (2010).
33. J. B. Hamard, R. Cireasa, B. Chatel, V. Blanchet, B. J. Whitaker, *J. Phys. Chem. A* **114**, 3167 (2010).
34. J. B. Bertrand *et al.*, *Phys. Rev. Lett.* **106**, 023001 (2011).

Acknowledgments: We thank A. Stolow for fruitful discussions and B. Whitaker and K. Takatsuka for permission to use information underlying Figs. 1 and 4C. We acknowledge financial support from the Swiss National Science Foundation (PPOOP2_128274), Agence Nationale de la Recherche (ANR-08-JCJC-0029 HarMoDyn), Centre National de la Recherche Scientifique (PICs: Imagerie moléculaire par impulsions attosecondes), National Sciences and Engineering Research Council of Canada, Canadian Institute for Photonic Innovations, and Air Force Office of Scientific Research.

Supporting Online Material

www.sciencemag.org/cgi/content/full/334/6053/208/DC1
Materials and Methods
Figs. S1 to S5
Tables S1 to S6
References (35–43)

20 May 2011; accepted 15 August 2011
10.1126/science.1208664

Conical Intersection Dynamics in NO₂ Probed by Homodyne High-Harmonic Spectroscopy

H. J. Wörner, J. B. Bertrand, B. Fabre, J. Higuët, H. Ruf, A. Dubrouil, S. Patchkovskii, M. Spanner, Y. Mairesse, V. Blanchet, E. Mével, E. Constant, P. B. Corkum and D. M. Villeneuve

Science **334** (6053), 208-212.
DOI: 10.1126/science.1208664

ARTICLE TOOLS

<http://science.sciencemag.org/content/334/6053/208>

SUPPLEMENTARY MATERIALS

<http://science.sciencemag.org/content/suppl/2011/10/12/334.6053.208.DC1>

RELATED CONTENT

<http://science.sciencemag.org/content/sci/334/6053/187.full>

REFERENCES

This article cites 42 articles, 6 of which you can access for free
<http://science.sciencemag.org/content/334/6053/208#BIBL>

PERMISSIONS

<http://www.sciencemag.org/help/reprints-and-permissions>

Use of this article is subject to the [Terms of Service](#)

Science (print ISSN 0036-8075; online ISSN 1095-9203) is published by the American Association for the Advancement of Science, 1200 New York Avenue NW, Washington, DC 20005. 2017 © The Authors, some rights reserved; exclusive licensee American Association for the Advancement of Science. No claim to original U.S. Government Works. The title *Science* is a registered trademark of AAAS.